Energy 212 (2020) 118779

Contents lists available at ScienceDirect

Energy

journal homepage: www.elsevier.com/locate/energy

Freestanding flexible multilayered Sulfur–Carbon nanotubes for Lithium–Sulfur battery cathodes

Won Yeol Lee [a], En Mei Jin [a, *], Jung Sang Cho [b], Dong-Won Kang [c], Bo Jin [d], Sang Mun Jeong [a, **]

[a] Department of Chemical Engineering, Chungbuk National University, Chungdae–ro 1, Seowon–Gu, Cheongju, Chungbuk, 28644, Republic of Korea
[b] Department of Engineering Chemistry, Chungbuk National University, Chungdae–ro 1, Seowon–Gu, Cheongju, Chungbuk, 28644, Republic of Korea
[c] School of Energy Systems Engineering, Chung–Ang University, Heukseok–ro 84, Dongjak–gu, Seoul, 06974, Republic of Korea
[d] Key Laboratory of Automobile Materials, Ministry of Education, and College of Materials Science and Engineering, Jilin University, Changchun, 130022, China

ARTICLE INFO

Article history:
Received 29 April 2020
Received in revised form
26 August 2020
Accepted 1 September 2020
Available online 6 September 2020

Keywords:
Lithium–sulfur batteries
Freestanding
Carbon nanotubes
Multilayer film electrodes
Flexible

ABSTRACT

A freestanding, flexible, multilayered sulfur–carbon nanotube film (MLSC) cathode was prepared for use in lithium–sulfur (Li–S) batteries without a metal current collector and binder using an economical and simple vacuum filtration method. The sulfur content in the MLSC electrode was maintained at 60 wt%. The MLSC electrode delivered a high initial reversible discharge capacity of 913 mAh g^{-1} and maintained a capacity of 736 mAh g^{-1}, indicating excellent capacity retention. In addition, the coulombic efficiency of the MLSC electrode was over 92% throughout the total cycling, demonstrating superior cycling stability. It exhibited the initial discharge capacities at 0.2 and 2C of 951 and 642 mAh g^{-1}, respectively, with 68% rate capability (2C/0.2C). These results indicate that the carbon nanotube film–wrapped structure of the MLSC electrode enables rapid electron transport in the electrode owing to its good electrical conductivity, and that it successfully suppresses the dissolution of lithium polysulfide in the electrolyte. Further, the MLSC electrode was stable during folding and bending in pouch cells.

1. Introduction

Currently, most energy consumption is dependent on fossil fuels leads to many social issues, such as environmental problems, energy supply insecurity, and price fluctuations [1]. To solve these social issues, conventional energy sources are being replaced by wind, tidal, and solar energy, which are eco–friendly renewable energy sources. The use of these renewable energy sources depends on environmental factors that restrict the locations and times when energy can be generated [2,3]. In addition, the rapid development of portable electronic devices and electric vehicles (EVs) is increasing the demand for high-performance energy storage materials [4].

Lithium–ion batteries (LIBs) are the most promising energy storage devices and are widely used in electronic devices, power tools, EVs, and energy storage systems (ESSs) owing to their high energy and power density, long cycle life, low self–discharge rate, and safety. Traditional LIBs that use metal oxides (such as LCO, LNO, NCA, and MCM) as the cathode material have high discharge rates and are safe, though such batteries are expensive and possess low energy densities [5–7]. Among these LiBs, lithium–sulfur (Li–S) batteries have garnered attention as promising next–generation ESSs for large–scale applications [8] because of their high theoretical capacity (1675 mAh g^{-1}) and energy density (2600 Wh kg^{-1}) [9–11]. In addition, sulfur is lightweight, abundant, non-toxic, and inexpensive [12,13]. Although Li–S batteries have many advantages, there are several problems that prevent their practical application. Based on the reaction mechanism and experimental results from multiple studies, the several factors have been identified that affect the electrochemical performance of Li–S batteries [14]. Firstly, the low electrical conductivity of sulfur (5×10^{-30} S cm^{-1}) results in low utilization of the active material (sulfur), and a low specific capacity [15,16]. Therefore, an appropriate amount of a conductive material is added in the active

* Corresponding author.
** Corresponding author.
E-mail addresses: dnjsduf22@naver.com (W.Y. Lee), jinenmei@chungbuk.ac.kr (E.M. Jin), jscho@chungbuk.ac.kr (J.S. Cho), kangdwn@cau.ac.kr (D.-W. Kang), jinbo@jlu.edu.cn (B. Jin), smjeong@chungbuk.ac.kr (S.M. Jeong).

https://doi.org/10.1016/j.energy.2020.118779
0360-5442/

material to ensure good electron transport, improve the utilization rate of the active material, enhance electrode dynamics, and improve cycle performance [17]. The second factor is the shuttle effect of lithium polysulfides (Li_2S_x, $2 < x \leq 8$), which are intermediate products in the multistep reaction of lithium and sulfur that are soluble in the electrolyte and shuttle between the cathode and anode. These intermediate polysulfides can pass though the separator and react with the lithium metal anode, resulting in corrosion of the anode and irreversible loss of active material [18,19]. One strategy to solve this problem is to trap sulfur in a structure of conductive carbon to improve electrical conductivity and prevent lithium polysulfide dissolution. Another factor is the volume expansion of sulfur during discharge [20]. The volume changes can result in an unstable mechanical structure of the electrode. If the electrode structure cracks, the active material will lose contact with the conductive agent, leading to capacity decay or battery failure. Flexible cathode materials are commonly used to buffer volume changes of the electrode. A partial sulfur–filled conductive agent is also used to avoid electrode structure damage. Many research groups use carbon nanotubes (CNTs) [21,22], carbon nanofibers [23,24], graphene [25,26], hollow carbon spheres [27,28], and porous carbon [29,30] as the conductive material to solve the aforementioned problems. Another way is to use conductive polymers, such as polyanilines, polypyrroles, and poly (3,4-ethylenedioxythiophene)-poly (styrenesulfonate) (PEDOT:PSS) [31–33], to increase conductivity and prevent lithium polysulfide dissolution. Tiwari et al. prepared a composite, which contains a sulfur-rich polymer and long cylindrical porous carbon nanotubes (LCNT) for lithium-sulfur batteries. The composite showed a high discharge capacity of 1040 mAh g^{-1} in the 1st cycle at 0.5C and 610 mAh g^{-1} after 200 cycles (59% capacity retention) [34]. Ren et al. also designed spherical double-layered hollow carbon/sulfur composite coated with a conductive layer of PEDOT:PSS. In this study, the PEDOT layer served as a protective layer to prevent dissolution of lithium polysulfides while increasing electrical conductivity of electrodes. As a result, the composite showed an initial discharge capacity of 1089 mAh g^{-1} at 0.2C and 590 mAh g^{-1} after 200th cycle (55% capacity retention) [35].

Currently, energy storage devices are increasingly required to be bendable and additionally foldable beyond a rigid shape, and the low production cost of devices is also important [36]. It means that the thinner and lower the weight of the electrodes in cells is more advantageous, and the synthetic process of electrodes should be simple and less time-consuming. The conventional slurry–coated electrode manufacturing for batteries includes metal (aluminum) current collectors and binders, which increases the battery price and the weight of the electrode. In addition, the manufacturing process is complex, and the thick coating cracks when the electrodes are bent, leaving the current collector poorly attached [37]. From the aforementioned point of view, the conventional slurry coating manufacturing method is not suitable for flexible electrodes. Therefore, a lot of studies have been recently conducted to synthesize free-standing electrodes that do not require both metal current collectors and binders [38]. This electrode manufacturing method can not only increase the sulfur content, but also improve the bending and folding characteristics. Methods for manufacturing freestanding electrodes include vacuum filtration [39,40] and electrospinning [41,42]. Köse et al. prepared flexible S/rGO/CNT composite as cathodes for lithium–sulfur batteries by vacuum filtration method. The composite exhibited an initial discharge capacity of 1150 mAh g^{-1} at 0.1C and 666 mAh g^{-1} after the 300th cycle (58% capacity retention) [40]. Gao et al. also prepared a freestanding flexible electrode for lithium-, and sodium ion batteries, in which MnS nanoparticles were embedded in carbon-matrixed nanofibers (MnS@CNF) obtained after electrospinning process [42]. The product exhibited specific capacities of 240 mAh g^{-1} at a current density of 5 A g^{-1} and 600 mAh g^{-1} at 200 mA g^{-1} with high rate performance when applied to lithium-ion battery anodes.

In this study, a freestanding, flexible, multilayered sulfur-carbon nanotube film (MLSC) electrode for an Li–S battery, without a metal current collector or binder, was prepared by vacuum filtration. This method is simple and enables easy control of the thickness, weight, cost, and sulfur content of the film. In addition, compared to the single–layered S–CNT electrode, the CNT-wrapped structure provides better conductivity, increases the electron transport speed during the charge–discharge processes, and suppresses the dissolution of lithium polysulfides in the electrolyte, owing to the multilayered structure-locking in sulfur. It also demonstrates the flexibility and stability of manufactured MLSC electrodes, thereby serving as a foundation for the development of foldable and wearable devices.

2. Experimental

2.1. Preparation of freestanding SLSC and MLSC electrode

CNTs (Multiwall type, Diameter: 20 nm, length: ~5 μm, Carbon Nano–material Technology Co., LTD) were used to prepare the CNT film with a simple vacuum filtration method. To prepare the film, the CNTs were dispersed in isopropanol (99.5%, Samchun chemical, Korea) via ultrasonication for 30 min. Then, the CNT solution was vacuum–filtered through filter paper (Advantec no. 2, Advantec) using an aspirator (A–1000S, EYELA). After filtration, the CNT film was dried in a vacuum at 60 °C for 12 h. Finally, the film was peeled off the filter paper to obtain a flexible CNT film. Three CNT films (approximately 40 μm thick) were prepared using this method, one of which was used to prepare an S–CNT film. To prepare the S–CNT film, sulfur powder (99.5%, Alfa Aesar) was dissolved in carbon disulfide (CS_2, anhydrous, ≥99%, Sigma–Aldrich), which became a clear, colorless liquid that was then dropped onto a CNT film. After drying at 70 °C for 1 h, the CS_2 solution was sprinkled on the S–CNT film again, which was then placed between the two CNT films as an interlayer. The multilayered S–CNT electrode (MLSC) was dried at 70 °C for 1 h to remove the CS_2 solution. After drying, the MLSC electrode was compressed to a thickness of 100 μm by a thermal roll press to reduce the contact resistance between the films. A schematic for the preparation of MLSC is presented in Scheme 1. A single layer S–CNT electrode (SLSC) was prepared in the same way, with the same thickness as the MLSC electrode, but without the outer CNT films. The sulfur content of the SLSC and MLSC electrodes was maintained at 60 wt%.

2.2. Coin cell assembly

For the CR2032 coin cell assembly, two as–prepared electrodes were punched into 1.6 cm diameter circles (effective area of 2 cm^2) to be used as cathodes. It should be emphasized that the cathodes did not contain any binders or collectors, such as Al or Cu foil. This is the primary difference between our electrodes and conventional electrode preparation methods. The cells were assembled in an argon–filled glove box with an oxygen and moisture level of less than 1 ppm. Lithium foil and polypropylene (PP, Celgard 2400, Celgard) were used as the counter electrode and separator, respectively. The electrolyte, 1 M bis(trifluoromethane) sulfonamide lithium salt (LiTFSI, $LiN(SO_2CF_3)_2$, Sigma–Aldrich) in a solvent mixture consisting of 1,3–dioxolane (DOL, Sigma–Aldrich) and 1,2–dimethoxyethane (DME, Sigma–Aldrich) (1:1, v/v) including the 0.1 M $LiNO_3$, was introduced into the Li–S batteries.

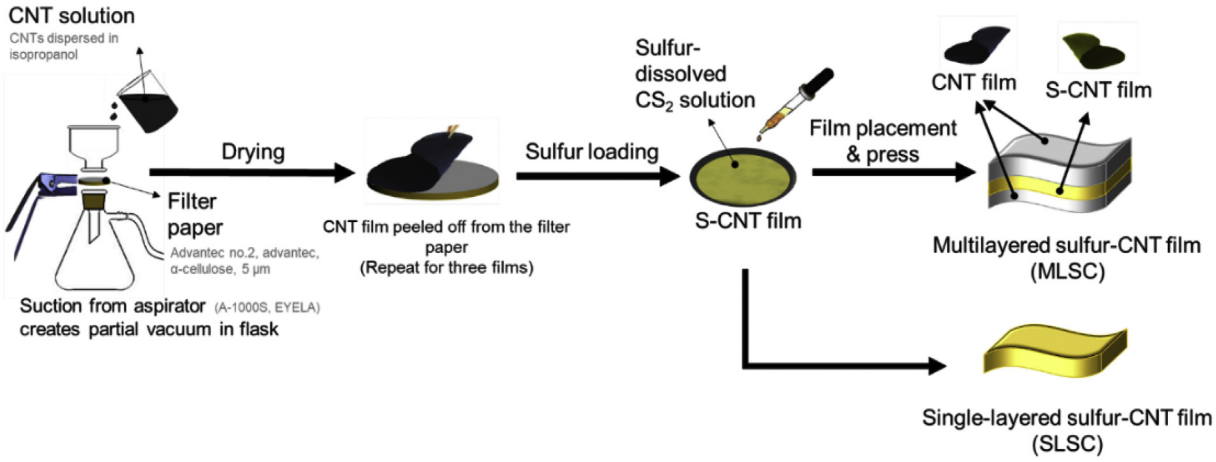

Scheme 1. Steps for preparing the SLSC and MLSC electrodes using a simple filtration method, subsequent recrystallization of the sulfur, and a press step.

For electrochemical tests, the manufactured coin cells were stabilized for 12 h.

2.3. Pouch cell assembly

The pouch cell was assembled in an argon–filled glove box with an oxygen and moisture level less than 1 ppm. The same counter electrode, separator, and electrolyte were used as in the coin cell. The active area of the MLSC electrode in the pouch cell was 1.6 × 4 cm. Lithium foil was cut to the same size as the MLSC electrodes. The MLSC electrodes and lithium foil were connected with aluminum and nickel tabs, respectively. The separator was placed in between the MLSC electrode and lithium foil as a sandwich, and then they were all sealed together using a pouch cell vacuum seal machine (VS–120J, J-Innotech, Korea).

2.4. Characteristic and measurements

The crystal structure was determined by X–ray diffraction (XRD, D8 Discover with GADDS) and field emission scanning electron microscopy (FE–SEM, Carl Zeiss, LEO–1530), and energy dispersive X–ray spectroscopy (EDS) was performed to examine the morphologies of the MLSC and SLSC electrodes. Cyclic voltammetry (CV), galvanostatic charge–discharge cycles (WonATech, WBCS3000L), and electrochemical impedance spectroscopy (EIS, Metrohm Autolab B.V., PGSTAT302N) were conducted to investigate the electrochemical properties of the battery. CV was carried out at a scanning rate of 0.1 mV s^{-1} within the voltage range of 1.7–2.8 V, and galvanostatic charge–discharge cycles were performed at 0.2C with a cut–off voltage of 1.7–2.8 V. EIS was performed in the frequency range of 0.01 Hz–100 kHz at an amplitude of 5 mV. All electrochemical measurements were acquired at 25 °C.

3. Results and discussion

To confirm the formation of sulfur in the CNT film, the XRD pattern of the S–CNT film was investigated and is shown in Fig. 1. The XRD pattern of the CNT film shows a broad peak at approximately 26°, which is attributed to amorphous carbon [43,44]. The characteristic sulfur peak can be easily seen in the XRD pattern of the S–CNT electrode after comparison with the JCPDS card no. 08–0247 (sulfur), indicating that the sublimed sulfur successfully recrystallized on the surface of or within the CNT film after the evaporation of CS_2.

The morphologies of the prepared SLSC and MLSC electrodes

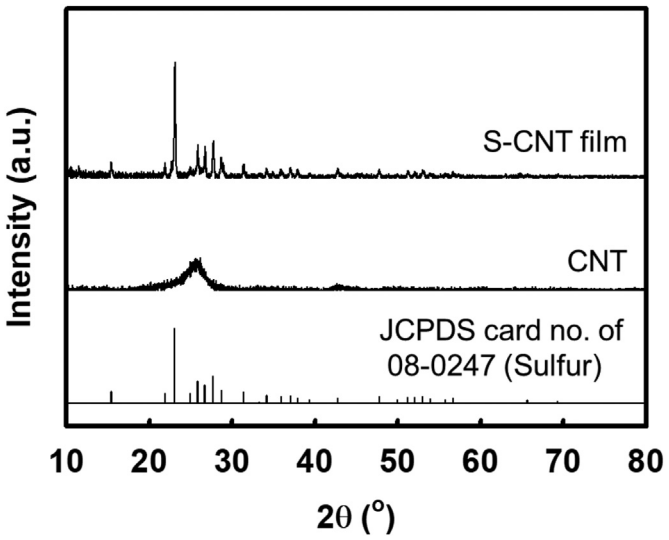

Fig. 1. XRD patterns of the S–CNT film.

were determined by FE–SEM images, as shown in Fig. 2. As shown in the cross–section images of the SLSC (Fig. 2a) and MLSC (Fig. 2b) electrodes, both electrodes have a uniform thickness of approximately 100 μm and no cracks, which indicates good contact between the CNT and S–CNT films. This implies that the preparation of the electrode was highly successful. In addition, the as–prepared SLSC electrode (Fig. 2a) shows a dense and uniform surface, indicating that the sulfur uniformly recrystallized on the surface and in the pores of the CNT film. The uniform distribution of sulfur in the CNT film should lead to good electron transport and excellent electrochemical properties. The MLSC electrode shows a scrim CNT structure, which easily absorbs the electrolyte into the internal S–CNT layer and prevents the lithium polysulfide from dissolving in the electrolyte, thereby suppressing anode (Li foil) corrosion and irreversible loss of active material. To determine a more accurate sulfur distribution and electrode structure, the MLSC electrode was stripped and subjected to an FE–SEM analysis along with C and S element mapping. Fig. 2c shows an FE–SEM image of the CNT–stripped MLSC electrode; the corresponding EDS mapping in Fig. 2d confirms the uniform distribution of sulfur in the S–CNT film and that both sides of the S–CNT film are completely covered by the CNT films. Because of this structure, the MLSC

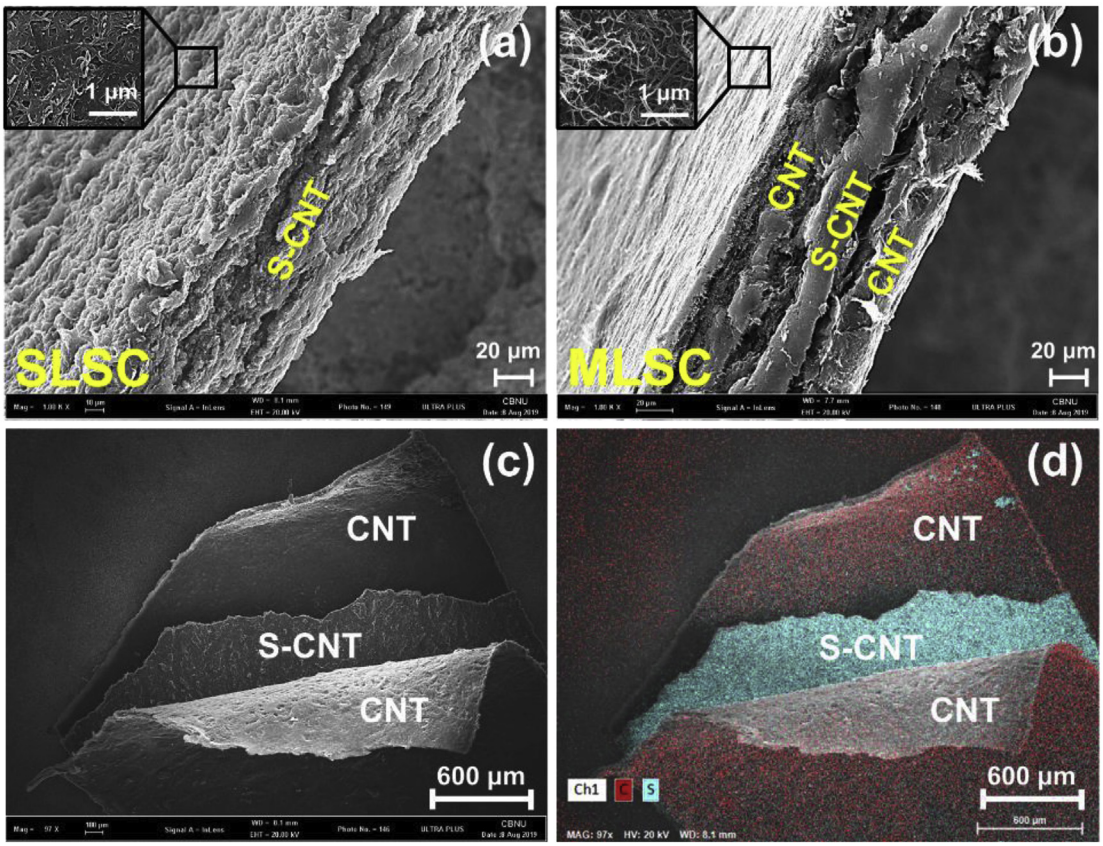

Fig. 2. FE–SEM images of the (a) SLSC electrode, (b) MLSC electrode, and (c) MLSC electrode with the CNT layer stripped off. (d) C and S element mapping image of the MLSC electrode.

electrode enables faster electron transport during the charge–discharge process and suppresses the dissolution of lithium polysulfides in the electrolyte. Smooth surfaces are apparent on the SLSC and MLSC electrodes.

To stabilize the batteries, the electrochemical performance of all batteries was tested after one charge and discharge cycle. The electrochemical properties of the different SLSC and MLSC electrodes for Li–S batteries were investigated by CV at 0.1 mV s^{-1}, as shown in Fig. 3a and b. In each cathodic scan, the SLSC and MLSC electrodes presented two prominent peaks at approximately 2.30 and 2.00 V, which correspond to the two discharge plateaus. The first peak at 2.30 V is related to the conversion of cyclo–S_8 to soluble long–chain lithium polysulfides (Li_2S_x, $4 \leq x \leq 8$), and the second reduction peak at 2.00 V is related to the conversion of long–chain lithium polysulfides to insoluble Li_2S_2 and Li_2S [45]. In the subsequent anodic scan, two distinct peaks were observed at 2.33 and 2.43 V, corresponding to the first conversion of insoluble reduction products into soluble long–chain lithium polysulfides and the final oxidation to elemental S, respectively [46]. In addition, the CV curves shifted slightly in the second cycle because of the transition of α–S_8 to β–S_8 at the end of the first cycle [47]. An almost identical curve track during the latter cycles indicates that the electrochemical process for the MLSC electrode is stable. To understand the interface charge transfer resistance of Li–S batteries with SLSC and MLSC electrodes, EIS Nyquist plots were obtained from 0.01 Hz to 100 kHz before cycling and after 100 cycles, as shown in Fig. 3c and d, respectively. The Nyquist plots were fitted with an equivalent circuit (inset of Fig. 3c and d) using the NOVA program (Version 1.10.4, Metrohm Autolab B.V.). Herein, R_s in the high–frequency region is the bulk resistance, R_{SEI} in the semicircle from high to medium frequency refers to the solid electrolyte interphase (SEI) (Li_2S_2 or Li_2S), R_{ct} in the semicircle at medium frequency is the charge transfer resistance at the cathode, and W is the Warburg impedance, which represents the impedance of lithium–ion diffusion in the electrodes [48]. *CPE1* and *CPE2* refer to the constant phase elements of the SEI and the electrode surface of the cathode, respectively [49]. As shown in Fig. 3c, both the electrodes display a single semicircle at high frequencies, which corresponds to the charge transfer resistance of the electrodes [50,51]. After 100 cycles, two semicircles are observed, which indicates the formation of the SEI film. The MLSC electrode shows smaller semicircles than the SLSC electrode both before cycling and after 100 cycles, which implies that the electrode resistance of the MLSC is lower than that of the SLSC electrode. The fitted EIS parameters are listed in Table 1. R_{SEI} and R_{ct} of the MLSC electrode have relatively low values of 9.4 and 16.5 Ω, respectively, after 100 cycles, suggesting that the MLSC electrode features superior electrochemical properties and rapid electron transport during the electrochemical Li^+ insertion/extraction reaction.

Fig. 4a and b shows typical charge–discharge profiles for Li–S batteries with SLSC and MLSC electrodes. Charge–discharge tests were performed at voltages ranging from 1.7 to 2.8 V and a rate of 0.2C. The two charge–discharge potential plateaus can be observed in the charge–discharge profiles; these correspond to the two–step reaction of sulfur during the discharge process, as demonstrated in the CV measurements. In the discharge process, the first potential plateau (at approximately 2.3 V) is related to the conversion of cyclo-S_8 into soluble long-chain lithium polysulfides (Li_2S_x, $4 \leq x \leq 8$), corresponding to a low theoretical capacity (418 mAh g^{-1}, 0.5 e S^{-1}). This process shows fast reaction rates due to the high

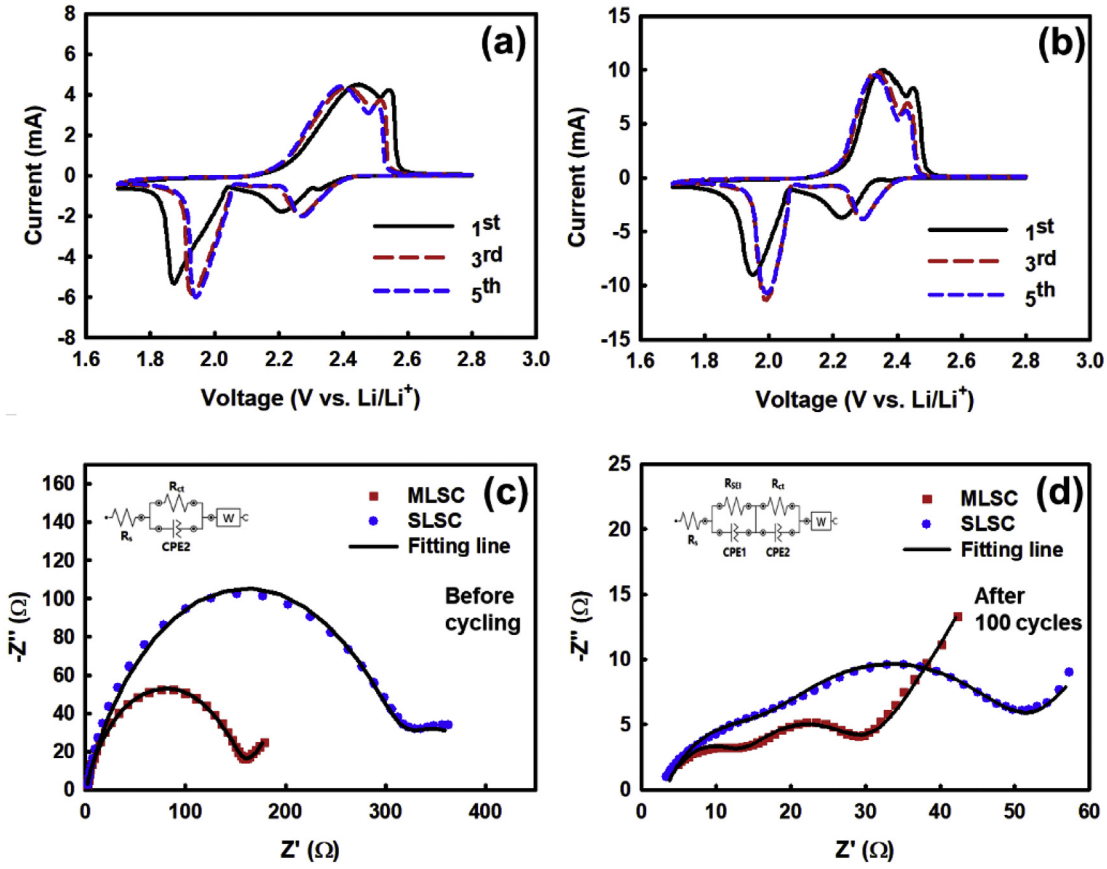

Fig. 3. CV of the (a) SLSC and (b) MLSC electrodes at different cycles, and Nyquist plot (c) before and (d) after 100 cycles.

Table 1
Fitted EIS parameters for Li−S batteries with SLSC and MLSC electrodes.

Electrodes	Cycle no.	R_s (Ω)	R_{SEI} (Ω)	R_{ct} (Ω)
SLSC	Before	2.4 (±0.1)	–	315.0 (±3)
	100th	3.4 (±0.1)	12.0 (±0.5)	36.0 (±0.5)
MLSC	Before	2.3 (±0.1)	–	155.0 (±3)
	100th	4.9 (±0.1)	9.4 (±0.1)	16.5 (±0.5)

solubility of long−chain lithium polysulfides. The second potential plateau (at approximately 2.0 V) is related to the conversion of the long-chain lithium polysulfides into insoluble Li_2S_2 and Li_2S, corresponding to a high theoretical capacity (1254 mAh g^{-1}, 1.5 e S^{-1}) [52]. Due to the conversion reaction between solids Li_2S_2 and Li_2S, the reactivity at this stage is much lower than that of the previous discharge plateau. Because this process is responsible for the overall capacity of the electrode, the discharge curves of the MLSC electrodes having long sections show a higher capacity compared to the SLSC electrodes. In the charge curve, the insoluble Li_2S_2 and Li_2S are reconverted into elemental S by the formation of intermediate lithium polysulfides [53]. Compared with the SLSC electrode, the MLSC electrode showed a higher initial charge and discharge capacity of 1124 and 913 mAh g^{-1}, respectively, with a first coulombic efficiency of 81%, and a capacity of 736 mAh g^{-1} after 100 cycles (a capacity retention of 81%). As shown in the cycling performance of the MLSC and SLSC electrodes (Fig. 4c), the MLSC has more stable cycling performance. However, the initial discharge capacity of the SLSC electrodes was relatively low, 808 mAh g^{-1}, and was 516 mAh g^{-1} after 100 cycles (a capacity retention of 64%). This confirms that the MLSC electrodes have better cycle stability than the SLSC electrodes, and it has been verified that the MLSC electrodes prevent the dissolution of some lithium polysulfides. Fig. 4d shows the rate performance of both cells at current densities of 0.2−2C. Again, the MLSC electrode exhibits a higher discharge capacity for all rate conditions than that the SLSC electrode. The reversible capacities of the MLSC electrode are 951, 812, 758, and 642 mAh g^{-1} at constant current rates of 0.2, 0.5, 1.0, and 2.0C, respectively, with 68% rate capability (2C/0.2C).

To verify the improved performance of the MLSC electrodes, a cycle test was conducted with an increase in sulfur loading. Fig. 4e shows the cycle performance as the sulfur loading increased from 2.00 to 3.85 mg cm^{-2}. For sulfur loading capacities of 2.00, 2.65, and 3.85 mg cm^{-2}, the electrodes had initial discharge capacities of 913, 880, and 837 mAh g^{-1} at 0.2C, and maintained discharge capacities of 736, 655, and 643 mAh g^{-1} after 100 cycles, respectively. Additionally, as shown in Fig. 4f, the area capacitance increases considerably as the amount of sulfur loading increases. They had high initial areal capacities of 1.83, 2.33, and 3.22 mAh cm^{-2} and maintained cycle performances of 1.47, 1.74, and 2.47 mAh cm^{-2} after 100 cycles, respectively. These values are shown in Table 2.

To confirm that the MLSC electrode can effectively prevent the dissolution of lithium polysulfides during the cycling, the morphology and elemental distribution of the MLSC electrode after 100 cycles was analyzed by FE−SEM and EDS mapping. As shown in the surface morphology mapping images of the SLSC electrode (Fig. 5a), the shape of the polysulfides on the surface after cycling is different than that before cycling (Fig. 2a). This is caused by the formation of polysulfides due to the reaction between sulfur and lithium on the surface [54]. This result proves that the capacity of the cycle is reduced because polysulfides dissolved in the

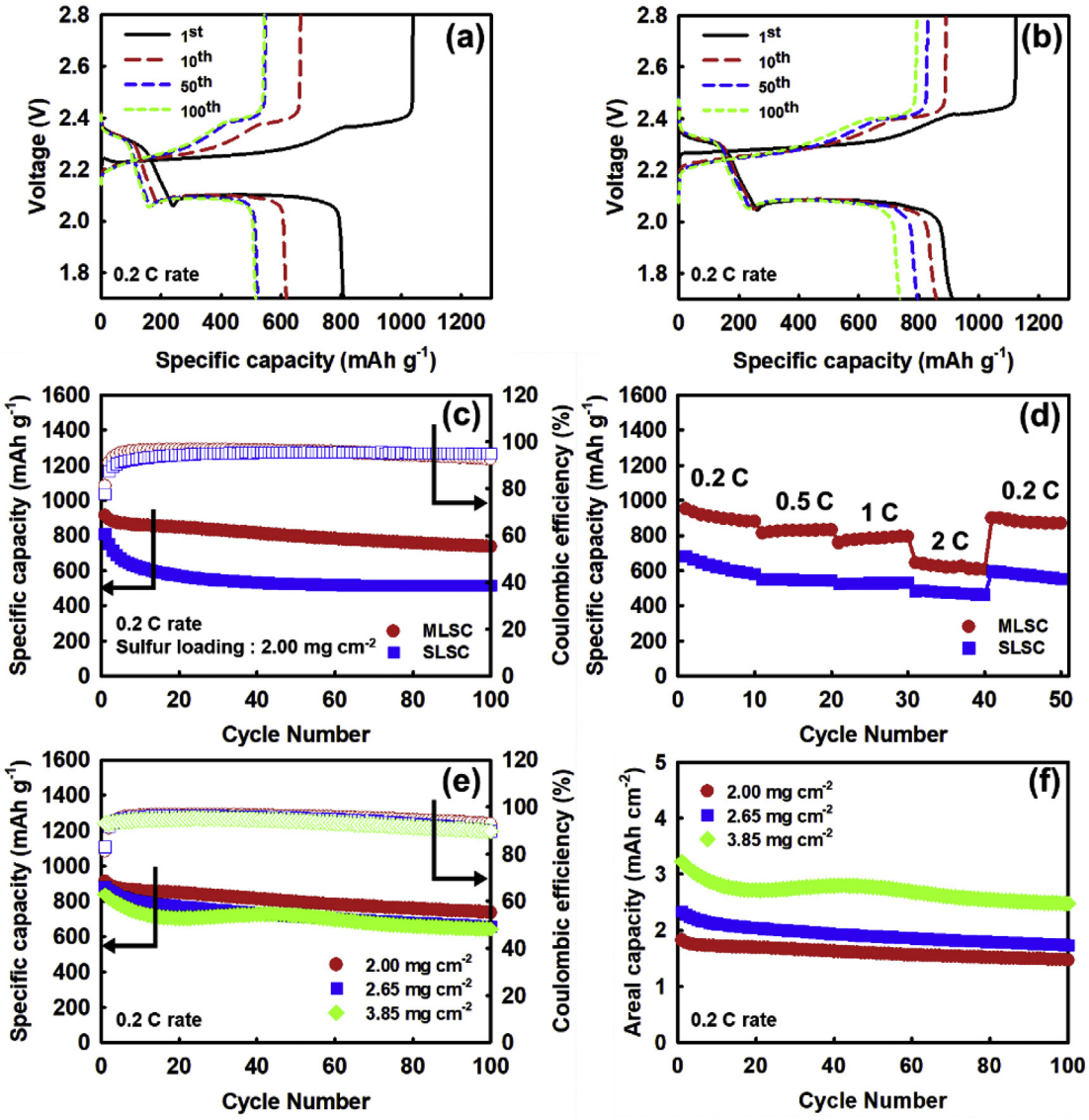

Fig. 4. Electrochemical performance of SLSC and MLSC electrode–based Li–S batteries; charge–discharge curves of (a) SLSC and (b) MLSC at different cycles; (c) cycling performance; (d) rate capability; (e) specific capacity with amount of sulfur loading; and (f) areal capacity with amount of sulfur loading.

Table 2
Discharge capacity, areal capacity, and cycle retention for Li–S batteries with SLSC and MLSC electrodes with amount of sulfur loading.

Electrodes	Sulfur loading (mg cm^{-2})	Discharge capacity at 0.2C (mAh g^{-1})		Areal capacity at 0.2C (mAh cm^{-2})		Capacity retention (%, 1–100th cycle)
		1st	100th	1st	100th	
MLSC	2.00	913	736	1.83	1.47	81
	2.65	880	655	2.33	1.74	74
	3.85	837	643	3.22	2.47	77
SLSC	2.00	808	516	1.62	1.03	64

electrolyte, which resulted in loss of active material. On the other hand, the surface of the MLSC electrode (Fig. 5b) does not show the shape of polysulfides. To observe the sulfur distribution on the electrode after 100th cycling, the cross–sectional EDS mapping was conducted. As shown in the mapping results, sulfur was mainly observed outside the SLSC electrode (Fig. 5a) due to diffusion by dissolution of lithium polysulfides, whereas sulfur (blue) of MLSC was evenly distributed between both sides of CNT layer even after 100th cycling (Fig. 5b). This indicates that the multilayer structure of electrode effectively prevents the dissolution of lithium polysulfides during the cycling. In addition, the solubility of lithium polysulfide was verified by visual inspection through a beaker cell test as shown in Fig. 5c and d. For the visual inspection, beaker cell was discharged at voltages ranging from 1.7 to 2.8 V with 0.1C for different period of time. As the discharging time increases, the color of the electrolyte tested with SLSC gradually turns dark yellow due to the dissolution of lithium polysulfides. The electrolyte with MLSC remained transparent, except around the electrode even after

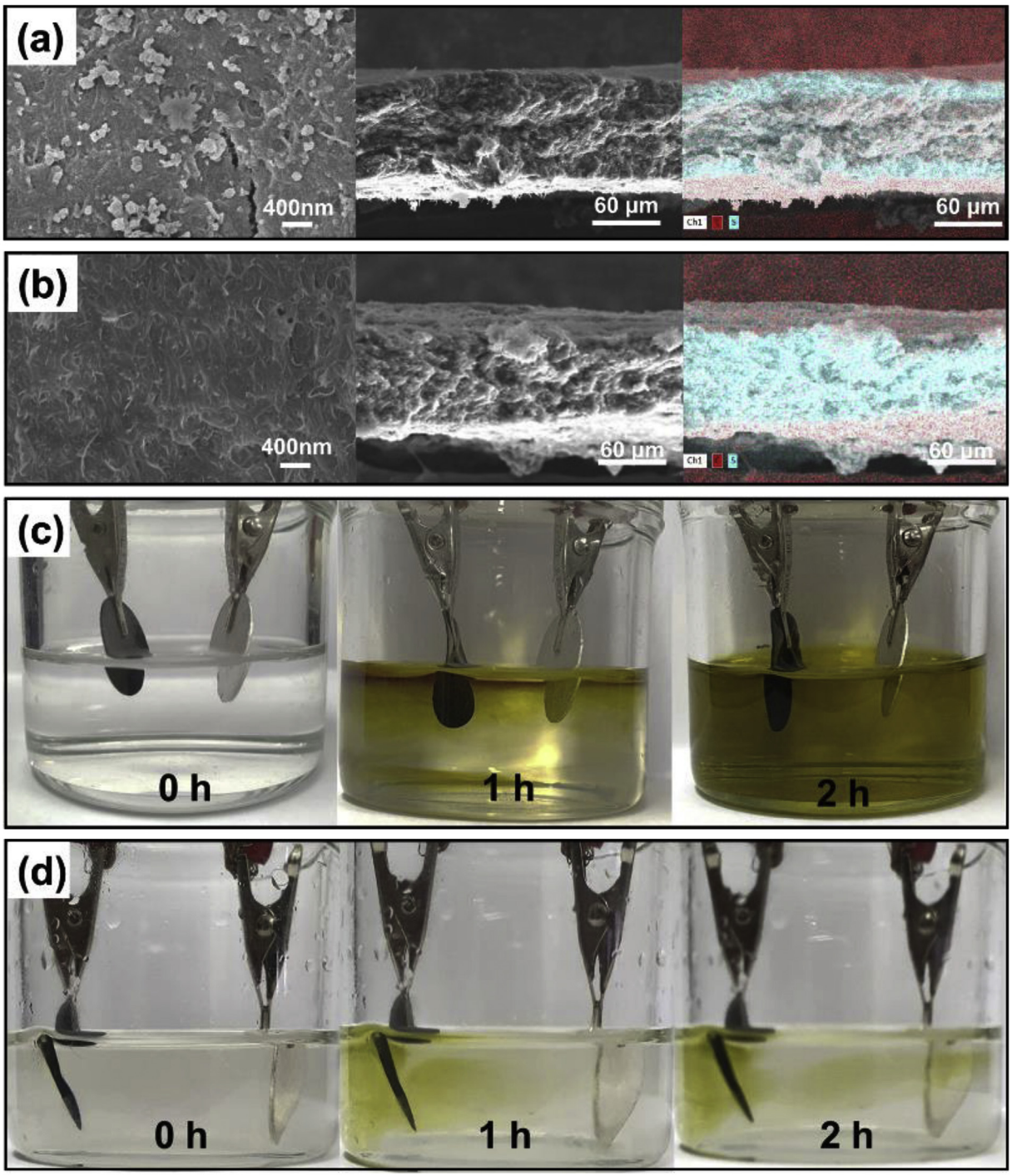

Fig. 5. Surface and cross-sectional FE–SEM and EDS (C and S elements) mapping images of the (a) SLSC and (b) MLSC electrodes after 100 cycles; images of the electrode lithium polysulfides dissolution of the (c) SLSC and (d) MLSC electrodes using beaker cells.

discharging for 2 h. This clearly demonstrates that the CNT layers on both sides of the active material effectively inhibited the dissolution of polysulfides.

A pouch cell was manufactured to confirm the flexibility and bending ability of the electrodes, as shown in Fig. 6. The highly flexible MLSC electrodes (Fig. 6a) were used to manufacture pouch cells with the structure shown in Fig. 6b. The charge–discharge test was conducted at voltages ranging from 1.7 to 2.8 V and a rate of 0.2C after folding the electrode 1 and 10 times. Discharge capacities of 930, 851, and 835 mAh g^{-1} were measured (Fig. 6c). Moreover, an LED was connected to the pouch cell to compare brightness in its original state, 90° folded, 180° folded, and recovered state after folding (Fig. 6d–g). Despite bending and unfolding the pouch cell, the LED lighting was bright enough to confirm that the flexible battery was well manufactured and that the MLSC electrodes are flexible and robust.

4. Conclusion

A freestanding, flexible, multilayered sulfur–carbon nanotube

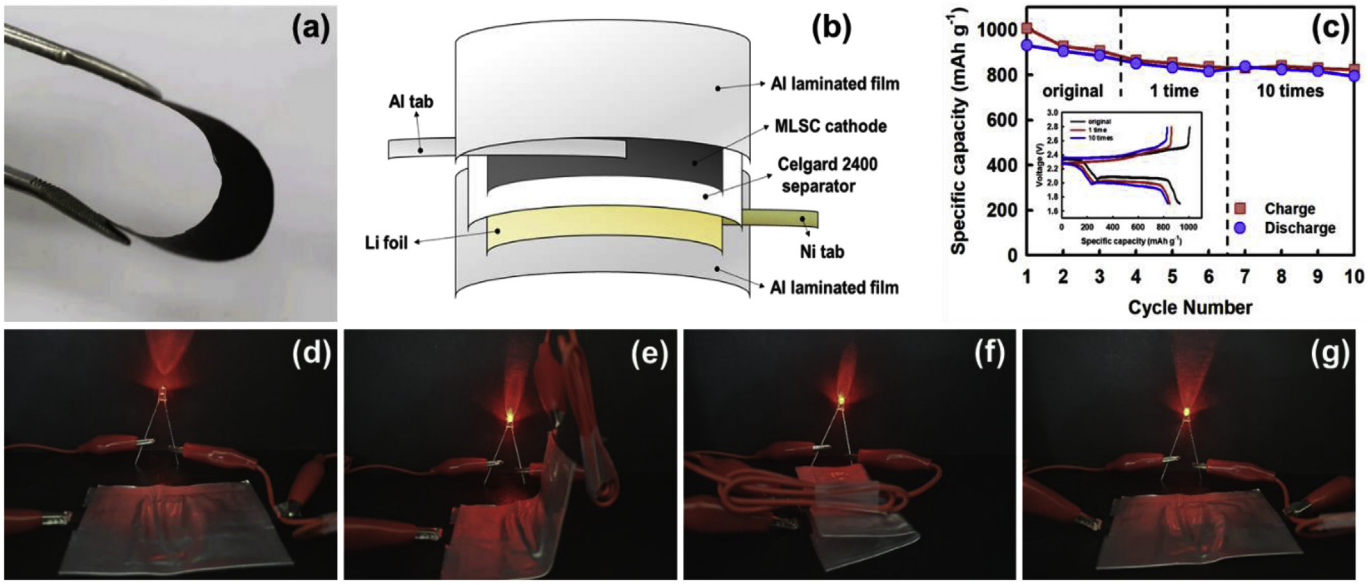

Fig. 6. (a) Photograph of a bent MLSC electrode, (b) pouch cell structure representation, (c) cycling performance of the MLSC electrode and after it was folded 1 and 10 times, and photographs of the flexible Li–S pouch cell (d) unfolded, (e) in a 90° fold, (f) in a 180° fold, and (g) after folding.

film (MLSC) used as electrode for Li–S batteries was successfully prepared using a simple vacuum filtration method. To prepare the MLSC electrode, three pieces of CNT film were prepared, and 60 wt % of sulfur was loaded into one of the CNT films. The freestanding, flexible MLSC exhibited excellent electrochemical properties compared with SLSC electrodes, such as a high initial reversible discharge capacity of 913 mAh g^{-1}, high rate capability (2C/0.2C, 68%), over 92% coulombic efficiency, and 81% capacity retention. The MLSC electrode before the cycle also had 155.0 Ω of R_{ct}, which is lesser than the 315.0 Ω R_{ct} of the SLSC electrode, and 16.5 Ω less than 36.0 Ω R_{ct} of the SLSC electrode after 100 cycles. Thus, the interfacial charge transfer of MLSC was improved. The charge–discharge of the pouch cell showed discharge capacities of 930, 851, and 835 mAh g^{-1} in its original state, after 1 fold, and after 10 folds, respectively. This indicates that the MLSC electrode was flexible and stable.

CREDIT author statement

Won Yeol Lee: Visualization, Investigation. En Mei Jin: Methodology, Data curation. Jung Sang Cho: Writing – Review & Editing. Dong-Won Kang: Writing – Review & Editing. Bo Jin: Writing – Review & Editing. Sang Mun Jeong: Conceptualization, Supervision

Declaration of competing interest

The authors declare that they have no known competing financial interests or personal relationships that could have appeared to influence the work reported in this paper.

Acknowledgment

This work was supported by a National Research Foundation of Korea (NRF) grant funded by the Korea Government (MSIT) (No.2018R1A4A1024691). Also, this research was supported by Chungbuk National University (2019).

References

[1] Yang C, Li P, Yu J, Zhao LD, Kong L. Approaching energy-dense and cost-effective lithium-sulfur batteries: from materials chemistry and price considerations. Energy 2020;201:117718. https://doi.org/10.1016/j.energy.2020.117718.
[2] Chu C, Kwon BW, Lee W, Kwon Y. Effect of temperature on the performance of aqueous redox flow battery using carboxylic acid functionalized alloxazine and ferrocyanide redox couple. Kor J Chem Eng 2019;36:1732–9. https://doi.org/10.1007/s11814-019-0374-z.
[3] Maria TCC, Daniel DA, Elisa TB. Locational impact and network costs of energy transition: introducing geographical price signals for new renewable capacity. Energy Pol 2020;142:111469. https://doi.org/10.1016/j.enpol.2020.111469.
[4] Ko HS, Park HW, Kim GJ, Lee JD. Electrochemical characteristics of lithium–excess cathode material ($Li_{1+x}Ni_{0.9}Co_{0.05}Ti_{0.05}O_2$) for lithium–ion batteries. Kor J Chem Eng 2019;36:620–4. https://doi.org/10.1007/s11814-019-0248-4.
[5] Chung SH, Chang CH, Manthiram A. Robust, ultra–tough flexible cathodes for high–energy Li–S batteries. Small 2016;12:939–50. https://doi.org/10.1002/smll.201503167.
[6] Kang H, Santhoshkumar P, Park J, Sim G, Nanthagopal M, Lee C. Glass ceramic coating on $LiNi_{0.8}Co_{0.1}Mn_{0.1}O_2$ cathode for Li-ion batteries. Kor J Chem Eng 2020;37:1131–9. https://doi.org/10.1007/s11814-020-0570-x.
[7] Kwak D, Lim WG, Shin K, Cheong I, Lee J, Joo J. Solid-state conversion of metal oleate precursors for the preparation of $LiNi_{1/3}Co_{1/3}Mn_{1/3}O_2$ as cathode material for lithium-ion batteries. Kor J Chem Eng 2020;37:1258–65. https://doi.org/10.1007/s11814-020-0537-y.
[8] Wang Z, Shen J, Liu J, Xu X, Liu Z, Hu R, Yang L, Feng Y, Liu J, Shi Z, Ouyang L, Yu Y, Zhu M. Self–supported and flexible sulfur cathode enabled via synergistic confinement for high–energy–density lithium–sulfur batteries. Adv Mater 2019:1902228. https://doi.org/10.1002/adma.201902228.
[9] Zhao Q, Zhu Q, Miao J, Zhang P, Xu B. 2D MXene nanosheets enable small–sulfur electrodes to be flexible for lithium–sulfur batteries. Nanoscale 2019;11:8442–8. https://doi.org/10.1039/c8nr09653h.
[10] Zhang L, Wang Y, Niu Z, Chen J. Advanced nanostructured carbon–based materials for rechargeable lithium–sulfur batteries. Carbon 2019;141:400–16. https://doi.org/10.1016/j.carbon.2018.09.067.
[11] Chen W, Lei T, Qian T, Lv W, He W, Wu C, Liu X, Liu J, Chen B, Yan C, Xiong J. A new hydrophilic binder enabling strongly anchoring polysulfides for high-performance sulfur electrodes in lithium-sulfur battery. Adv Energy Mater 2018;8:1702889. https://doi.org/10.1002/aenm.201702889.
[12] Gueon D, Hwang J, Yang S, Cho E, Sohn K, Yang DK, Moon J. Spherical macroporous carbon nanotube particles with ultrahigh sulfur loading for Lithium–Sulfur battery cathodes. ACS Nano 2018;12:226–33. https://doi.org/10.1021/acsnano.7b05869.
[13] Yang H, Li Q, Guo C, Naveed A, Yang J, Nuli Y, Wang J. Safer lithium–sulfur battery based on nonflammable electrolyte with sulfur composite cathode. Chem Commun 2018;54:4132–5. https://doi.org/10.1039/C7CC09942H.
[14] Li F, Liu Q, Hu J, Feng Y, He P, Ma J. Recent advances in cathode materials for rechargeable lithium–sulfur batteries. Nanoscale 2019;11:15418–39. https://doi.org/10.1039/c9nr04415a.

[15] He J, Chen Y, Manthiram A. MOF–derived cobalt sulfide grown on 3D graphene foam as an efficient sulfur host for long–life lithium–sulfur batteries. iScience 2018;4:36–43. https://doi.org/10.1016/j.isci.2018.05.005.

[16] Xu N, Qian T, Liu X, Liu J, Chen Y, Yan C. Greatly suppressed shuttle effect for improved lithium sulfur battery performance through short chain intermediates. Nano Lett 2017;17:538–48. https://doi.org/10.1021/acs.nanolett.6b04610.

[17] Wang J, Qin W, Zhu X, Teng Y. Covalent organic frameworks (COF)/CNT nanocomposite for high performance and wide operating temperature lithium–sulfur batteries. Energy 2020;199:117372. https://doi.org/10.1016/j.energy.2020.117372.

[18] Yu M, Wang Z, Wang Y, Dong Y, Qiu J. Freestanding flexible Li_2S paper electrode with high mass and capacity loading for high–energy Li–S batteries. Adv Energy Mater 2017;7:1700018. https://doi.org/10.1002/aenm.201700018.

[19] Lin J, Zhang K, Zhu Z, Zhang R, Li N, Zhao C. CoP/C nanocubes-modified separator suppressing polysulfide dissolution for high-rate and stable Lithium–Sulfur batteries. ACS Appl Mater Interfaces 2020;12:2497–504. https://doi.org/10.1021/acsami.9b18723.

[20] Li X, Ding K, Gao B, Li Q, Li Y, Fu J, Zhang X, Chu PK, Huo K. Freestanding carbon encapsulated mesoporous vanadium nitride nanowires enable highly stable sulfur cathodes for lithium–sulfur batteries. Nanomater Energy 2017;40:655–62. https://doi.org/10.1016/j.nanoen.2017.09.018.

[21] Chen D, Yue XY, Li XL, Bao J, Qiu QQ, Wu XJ, Zhang X, Zhou YN. Freestanding double-layer MoO_3/CNT@S membrane: a promising flexible cathode for Lithium–Sulfur batteries. ACS Appl Mater Interfaces 2020;12:2354–61. https://doi.org/10.1021/acsami.9b17200.

[22] Zhang Q, Huang N, Huang Z, Cai L, Wu J, Yao X. CNTs@S composite as cathode for all-solid-state lithium-sulfur batteries with ultralong cycle life. J Energy Chem 2020;40:151–5. https://doi.org/10.1016/j.jechem.2019.03.006.

[23] Li H, Wang X, Qi C, Zhao C, Fu C, Wang L, Liu T. Self-assembly of MoO_3-decorated carbon nanofiber interlayers for high-performance lithium–sulfur batteries. Phys Chem Chem Phys 2020;22:2157–63. https://doi.org/10.1039/c9cp06287d.

[24] Chen X, Yuan L, Hao Z, Liu X, Xiang J, Zhang Z, Huang Y, Xie J. Free–standing Mn_3O_4@CNF/S paper cathodes with high sulfur loading for lithium–sulfur batteries. ACS Appl Mater Interfaces 2018;10:13406–12. https://doi.org/10.1021/acsami.7b18154.

[25] Chuang CC, Hsieh YY, Chang WC, Tuan HY. Phosphorus-sulfur/graphene composites as flexible lithium-sulfur battery cathodes with super high volumetric capacity. Chem Eng J 2020;387:123904. https://doi.org/10.1016/j.cej.2019.123904.

[26] Carbone L, Castillo A, Panda J, Pugliese G, Scarpellini A, Bonaccorso F, Pellegrini V. A high-sulfur-content graphene-based composite through ethanol evaporation for high-energy lithium-sulfur battery. ChemSusChem 2020;13:1593–602. https://doi.org/10.1002/cssc.201902305.

[27] Cai J, Zhang Z, Yang S, Min Y, Yang G, Zhang K. Self–conversion templated fabrication of sulfur encapsulated inside the N–doped hollow carbon sphere and 3D graphene frameworks for high–performance lithium–sulfur batteries. Electrochim Acta 2019;295:900–9. https://doi.org/10.1016/j.electacta.2018.11.013.

[28] Li X, Pan Z, Li Z, Zhong Y, Wang X, Xu M, Liao Y, Xing L, Qiu Y, Li W. Functionalized N–doped hollow carbon spheres as sulfur host with enhanced electrochemical performances of lithium–sulfur batteries. Ionics 2018;25:503–11. https://doi.org/10.1007/s11581-018-2729-6.

[29] Chen M, Jiang S, Cai S, Wang X, Xiang K, Ma Z, Song P, Fisher AC. Hierarchical porous carbon modified with ionic surfactants as efficient sulfur hosts for the high–performance lithium–sulfur batteries. Chem Eng J 2017;313:404–14. https://doi.org/10.1016/j.cej.2016.12.081.

[30] Li F, Qin F, Zhang K, Fang J, Lai Y, Li J. Hierarchically porous carbon derived from banana peel for lithium sulfur battery with high areal and gravimetric sulfur loading. J Power Sources 2017;362:160–7. https://doi.org/10.1016/j.jpowsour.2017.07.038.

[31] Wang J, Zhang S. Synthesis of polyaniline-sulfur composites with different nanostructures via an interfacial emulsification method and a micelle template method and their properties. RSC Adv 2020;10:11455. https://doi.org/10.1039/D0RA00122H.

[32] Kim J, Elabd A, Chung SY, Coskun A, Choi J. Covalent triazine frameworks incorporating charged polypyrrole channels for high-performance lithium–sulfur batteries. Chem Mater 2020;32:4185–93. https://doi.org/10.1021/acs.chemmater.0c00246.

[33] Ahn S, Noguchi T, Momma T, Nara H, Yokoshima T, Togasaki N, Osaka T. Facile fabrication of sulfur/Ketjenblack-PEDOT:PSS composite as a cathode with improved cycling performance for lithium sulfur batteries. Chem Phys Lett 2020;749:137426. https://doi.org/10.1016/j.cplett.2020.137426.

[34] Tiwari VK, Song H, Oh Y, Jeong Y. Synthesis of sulfur-co-polymer/porous long carbon nanotubes composite cathode by chemical and physical binding for high performance lithium-sulfur batteries. Energy 2020;195:117034. https://doi.org/10.1016/j.energy.2020.117034.

[35] Ren Y, Hu J, Zhong H, Zhang L. Multiple core-shelled sulfur composite based on spherical double-layered hollow carbon and PEDOT:PSS as cathode for lithium-sulfur batteries. J Alloys Compd 2020;837:155498. https://doi.org/10.1016/j.jallcom.2020.155498.

[36] Mao Y, Li G, Guo Y, Li Z, Liang C, Peng X, Lin Z. Foldable interpenetrated metal–organic frameworks/carbon nanotubes thin film for lithium–sulfur batteries. Nat Commun 2017;8:14628. https://doi.org/10.1038/ncomms14628.

[37] Qi C, Cai M, Li Z, Jin J, Chowdari BVR, Chen C, Wen Z. Ultrathin TiO_2 surface layer coated TiN nanoparticles in freestanding film for high sulfur loading Li-S battery. Chem Eng J 2020;399:125674. https://doi.org/10.1016/j.cej.2020.125674.

[38] Yu M, Ma J, Xie M, Song H, Tian F, Xu S, Zhou Y, Li B, Wu D, Qiu H, Wang R. Freestanding and sandwich–structured electrode material with high areal mass loading for long–life lithium–sulfur batteries. Adv Energy Mater 2017;7:1602347. https://doi.org/10.1002/aenm.201602347.

[39] Kim J, Kang Y, Song SW, Suk J. Freestanding sulfur–graphene oxide/carbon composite paper as a stable cathode for high performance lithium–sulfur batteries. Electrochim Acta 2019;299:27–33. https://doi.org/10.1016/j.electacta.2018.12.165.

[40] Köse H, Kurt B, Dombaycıoğlu Ş, Aydın A. Rational design of cathode structure based on free-standing S/rGO/CNT nanocomposite for Li-S batteries. Synth Met 2020;267:116471. https://doi.org/10.1016/j.synthmet.2020.116471.

[41] Zhang YZ, Zhang Z, Liu S, Li GR, Gao XP. Free–standing porous carbon nanofiber/carbon nanotube film as sulfur immobilizer with high areal capacity for lithium–sulfur battery. ACS Appl Mater Interfaces 2018;10:8749–57. https://doi.org/10.1021/acsami.8b00190.

[42] Gao S, Chen G, Dall'Agnese Y, Wei Y, Gao Z, Gao Y. Flexible MnS–carbon fiber hybrids for lithium–ion and sodium–ion energy storage. Chemistry 2018;24:13535–9. https://doi.org/10.1002/chem.201801979.

[43] Hwang JY, Kim HM, Sun YK. Controlling the wettability between freestanding electrode and electrolyte for high energy density lithium–sulfur batteries. J Electrochem Soc 2018;165:A5006–13. https://doi.org/10.1149/2.0131801jes.

[44] Zhang X, Zhou Y, Mao Y, Wei M, Chu W, Huang K. Rapid synthesis of ultrafine $NiCo_2O_4$ nanoparticles loaded carbon nanotubes for lithium ion battery anode materials. Chem Phys Lett 2019;715:278–83. https://doi.org/10.1016/j.cplett.2018.11.053.

[45] Zhou G, Wang DW, Li F, Hou PX, Yin L, Liu C, Lu GQ, Gentle IR, Cheng HM. A flexible nanostructured sulphur–carbon nanotube cathode with high rate performance for Li–S batteries. Energy Environ Sci 2012;5:8901. https://doi.org/10.1039/c2ee22294a.

[46] Zhang Z, Li Q, Zhang K, Chen W, Lai Y, Li J. Titanium–dioxide–grafted carbon paper with immobilized sulfur as a flexible free–standing cathode for superior lithium–sulfur batteries. J Power Sources 2015;290:159–67. https://doi.org/10.1016/j.jpowsour.2015.05.010.

[47] Conder J, Bouchet R, Trabesinger S, Marino C, Gubler L, Villevieille C. Direct observation of lithium polysulfides in lithium–sulfur batteries using operando X–ray diffraction. Nat Energy 2017;2:17069. https://doi.org/10.1038/nenergy.2017.69.

[48] Zhou G, Paek E, Hwang GS, Manthiram A. Long–life Li/polysulphide batteries with high sulphur loading enabled by lightweight three–dimensional nitrogen/sulphur–codoped graphene sponge. Nat Commun 2015;6:7760. https://doi.org/10.1038/ncomms8760.

[49] Lee J, Choi W. Surface modification of sulfur cathodes with PEDOT:PSS conducting polymer in lithium–sulfur batteries. J Electrochem Soc 2015;162:A935–9. https://doi.org/10.1149/2.0651506jes.

[50] Nobili F, Tossici R, Marassi R, Croce F, Scrosati B. An AC impedance spectroscopic study of Li_xCoO_2 at different temperatures. J Phys Chem B 2002;106:3909–15. https://doi.org/10.1021/jp013569a.

[51] Tang X, Gao F, Zou C, Yao K, Hu W, Wik T. Load-responsive model switching estimation for state of charge of lithium-ion batteries. Appl Energy 2019;238:423–34. https://doi.org/10.1016/j.apenergy.2019.01.057.

[52] Wang DW, Zeng Q, Zhou G, Yin L, Li F, Cheng HM, Gentle IR, Lu GQM. Carbon-sulfur composites for Li-S batteries; status and prospects. J Mater Chem 2013;1:9382. https://doi.org/10.1039/c3ta11045a.

[53] Fang R, Zhao S, Sun Z, Wang DW, Cheng HM, Li F. More reliable lithium-sulfur batteries: status, solutions and prospects. Adv Mater 2017;29:1606823. https://doi.org/10.1002/adma.201606823.

[54] She ZW, Yu JH, Li W, Hsu PC, Wang H, Sun Y, Yao H, Zhang Q, Cui Y. Two-dimensional layered transition metal disulphides for effective encapsulation of high-capacity lithium sulphide cathodes. Nat Commun 2014;5:5017. https://doi.org/10.1038/ncomms6017.